


Emergence of Power-Law Particle Size Distribution in Microfluidic Calcium Carbonate Precipitation: An Extended Yule Process with a Ripening Effect

Jianping Xu^{1,2,*} and Matthew T. Balhoff^{1,2}

¹*Hildebrand Department of Petroleum and Geosystems Engineering, The University of Texas at Austin, Austin, Texas 78712, USA*

²*Center for Subsurface Energy and the Environment, The University of Texas at Austin, Austin, Texas 78712, USA*

 (Received 19 September 2022; revised 12 January 2023; accepted 28 June 2023; published 17 July 2023)

Precipitation of calcium carbonate in bulk solutions is well known to result in a bell-shaped or bimodal particle size distribution. However, it is unclear how the distribution behaves if precipitation occurs in a small, confined volume. In this Letter, we conduct microfluidic experiments where sodium carbonate and calcium chloride solutions are continuously injected into a microchannel to precipitate calcium carbonate particles. Results show that, regardless of the variations in reagent concentrations, mixing schemes, flow rates, and precipitation time, sizes of precipitated particles in the channel are power law distributed, with an exponent of 1.4. The data are described by an extended Yule process with the introduction of a ripening term. Since the Yule process is a general mechanism for power law generation, the extended Yule process proposed here provides a general model for systems where growth and ripening simultaneously present.

DOI: 10.1103/PhysRevLett.131.034001

Calcium carbonate is an important mineral for nature and life. It is essential for the carbonate-silicate geochemical cycle [1,2] that dictates Earth's climate at geological timescales. It is also the main constituent of skeletal structures in living creatures such as echinoderm [3] and sponge [4]. It is ubiquitous in human society, including the paper and plastics industry [5], agriculture [5], pharmaceuticals [6], and fossil fuel energy [7].

Given its many applications, calcium carbonate is arguably the most studied mineral; however, our understanding of it is far from complete. For example, calcium carbonate precipitation in small, confined volumes, which holds the key to biomineralization [8–10], geological carbon sequestration [11,12], nanomaterial fabrication [13], etc., remains a challenging area. Extensive efforts have been made to unveil how confinements (e.g., organisms [9,10], porous media, and microfluidic devices [14–18]) shape the kinetics of precipitation [19,20], polymorphism [21], reactive transport mechanisms [15–17,20,22,23], spatial patterns of precipitates [24,25], and crystal morphologies [26–28]. An often-overlooked aspect is the statistics of precipitates. Since it is well known that calcium carbonate precipitation in bulk conditions results in a bell-shaped or bimodal particle size distribution [29–32], a natural question is, what size distribution is formed in confinements? To our knowledge, there is not yet any study that addresses this question.

In this Letter, we inject Na_2CO_3 and CaCl_2 solutions into a microfluidic channel to precipitate CaCO_3 . Microscopic images of the precipitates are analyzed to yield particle size statistics. Experimental conditions vary in multiple ways, but surprisingly all data collapse to a power-law

distribution with an exponent of 1.4. Although power-law distribution is ubiquitous in nature and society [33–35], this is the first time it is observed in mineral precipitation. An important factor contributing to its emergence is that supersaturation in confinement depletes quickly [28] and a continuous supply of reactants is required to fuel crystal growth. Furthermore, a finite feed rate renders competition for resources. These features are characteristic of dissipative systems such as growing networks [36,37] and economic incomes [38] that are ruled by power-law distributions.

Quantitatively, we find the data can be described by an extended version of the Yule process. The Yule process was proposed in 1925 to explain the observation that the number of species in a biologic genus follows a power-law distribution [39]. In the following decades it had been generalized to explain power-law distributions of city sizes [40], citations of academic papers [41], and internet weblinks [42]. It is one of the widely accepted mechanisms for power law generation (among others such as self-organized criticality [35] and phase transition [33,43]). However, in both the original and generalized Yule processes, the power exponent is larger than 2, which does not explain an exponent of 1.4. We show that introduction of a ripening term into the Yule process may resolve this issue. In the Letter we use “crystal” and “particle” interchangeably.

Schematics of the experimental setups and dimensions of the microfluidic chips are presented in Fig. 1. Details of chip fabrication are described in the Supplemental Material [44].

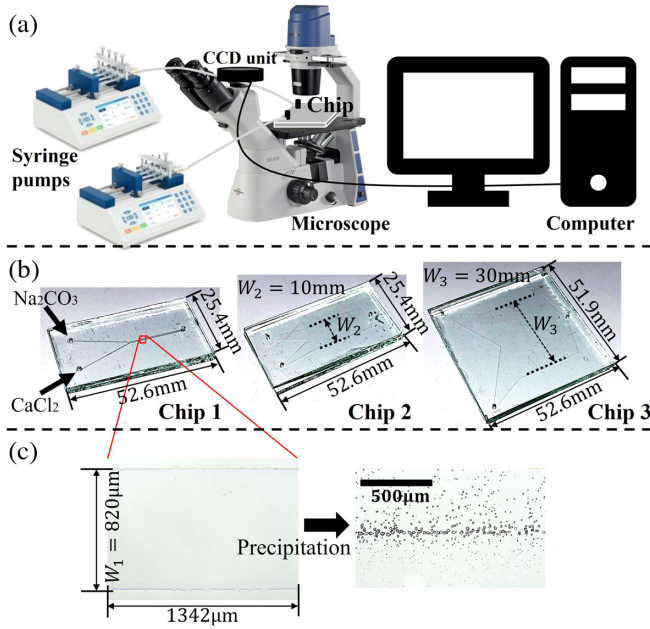


FIG. 1. (a) Schematics of experimental setups. The syringe pumps (Chemyx Fusion 400) inject reagents into the chip, which is monitored by the microscope (AccuScope EXI-310). The computer controls image acquisition through the microscope's CCD camera unit. (b) Dimensions of the three glass chips. Width and depth of the channels in chip 1, 2, 3 are 820 and 10 μm , 10 mm and 20 μm , 30 mm and 20 μm , respectively. (c) Microscopic view of the channel in chip 1. After precipitation, the channel is populated by crystal particles.

We conducted ten precipitation experiments (numbered Expt. 1–10) in chip 1, two (Expt. 11–12) in chip 2 and two (Expt. 13–14) in chip 3, all at room conditions. As described in Fig. 1, from chip 1 to chip 2 and 3,

cross-sectional area of the channel increases significantly, which models the ease of spatial confinement. Therefore, experiments in chips 2 and 3 would indicate if the power-law distribution returns to bimodal when confinement is reduced. Experimental conditions, including reagent concentrations (wt.%), injection rates ($\mu\text{L}/\text{h}$), precipitation time (hours) and mixing schemes, are varied to mimic real-world situations where fluids can mix and precipitate in various ways. Three mixing schemes (co-injection, prenuclei, and alternating) are employed. In co-injection, channels are initially saturated by water, and the reagents are simultaneously injected into the channel at equal and constant rates. In prenuclei, initially the channels are saturated with Na_2CO_3 solution. Then CaCl_2 solution is injected to displace the former, which creates nuclei. Following this, co-injection of the two is implemented. In alternating, injection rates of the two reagents are unequal and alternated between 1 and 20 $\mu\text{L}/\text{h}$. For simplicity the schemes are labeled as *c* (co-injection), *p* (prenuclei), and *a* (alternating).

Snapshots of Expt. 1–14 are shown in Fig. 2. We label experimental conditions and time in the figure in a format of (concentration, injection rate, mixing scheme, time). For example, (5, 2, c, 20.64) means 5 wt.% reagents, injection rates of 2 $\mu\text{L}/\text{h}$, co-injection scheme, image taken at 20.64 h. Precipitation at different locations of the channel is also examined. Size of a particle is measured by the pixel areas it occupies. Details of the particle analysis are presented in the Supplemental Material [44], which also includes a discussion of the impact of calcium carbonate polymorphic transition [45–47] on particle analysis.

Another factor that impacts particle size calculations is merger, as shown in Fig. 2(J.1). Since the particle analysis

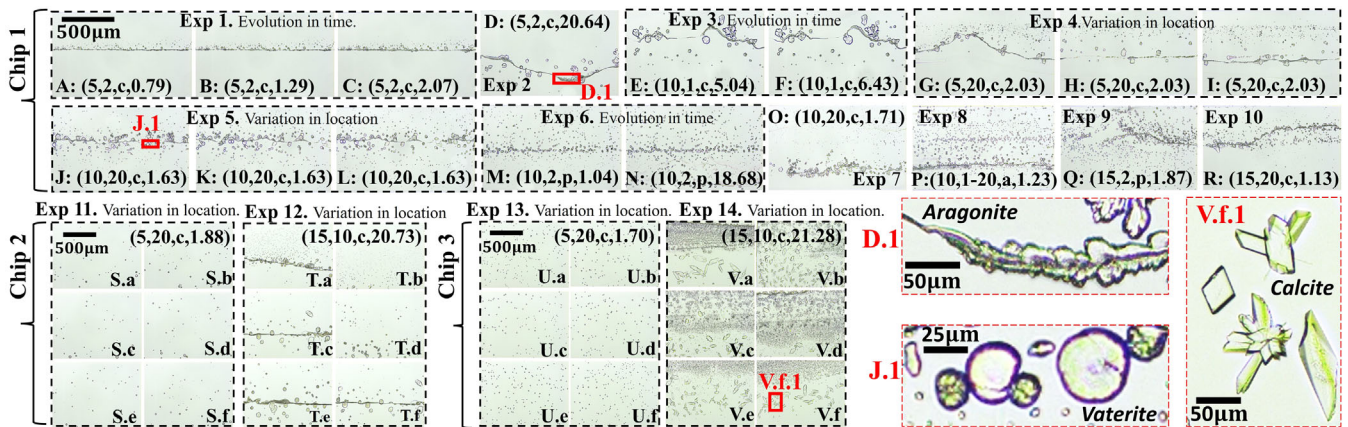


FIG. 2. Snapshots of precipitated calcium carbonate crystals in the three microfluidic chips. Grouped images are from the same experiment but taken at different locations in the channel or time. Insets (J.1) and (V.f.1) show the characteristic spherical vaterite and rhombohedral calcite [27,48–50]. (D.1) shows the elongated aragonite crystal, which extends to a long, serpentine structure, as evidenced in D, E, F, G, H, I, T.c, T.e, and T.f. Such continuous linelike aragonite structure is also observed in Yoon *et al.* [15]. Note that in batch or bulk conditions aragonite emerges when temperature exceeds 60 $^{\circ}\text{C}$ [45,51]. However, confinement promotes its formation at room temperature [52]. This is supported by our observations—in chip 3 that has the least confinement, there is no serpentine aragonite as found in chips 1 and 2.

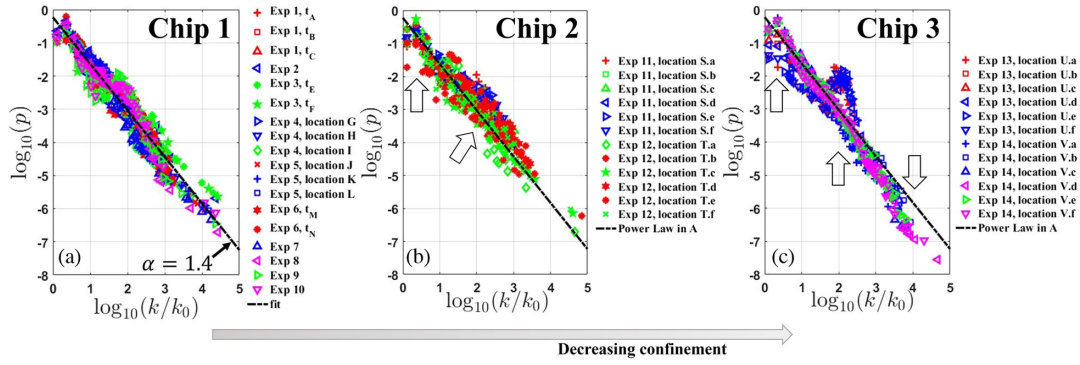


FIG. 3. The logarithm of fraction p of particles with area k versus the logarithm of dimensionless particle size k/k_0 , generated from experimental data in chip 1 [(a), Expt. 1–10], chip 2 [(b), Expt. 11 and 12], and chip 3 [(c), Expt. 13 and 14]. Labeling of time and location in the legends follows that in Fig. 2. The hollow arrows point to deviations from the power-law trend obtained in (a).

is based on image binarization [44], a merger is identified as one particle. In experiments such as Expt. 4, 6, 11, 13, merger seems rather scarce, while in Expt. 5, 7, 14, there are a few instances. In addition, in earlier times when particles are smaller, merger is less likely. As will be shown later, considering these variations, all data from chip 1 (Expt. 1–10) obey the same power-law distribution, indicating that merger is not essential for the power law. Also note that the starlike calcite in Fig. 2(V.f.1) (which also presents in, e.g., Figs. 2(E), 2(F), 2(V.a), and 2(V.e)) is not the result of merger. It grew from a nucleus with a heterogeneous structure. Close-up views of starlike calcites in Figs. 2(E), 2(F), 2(V.a), and 2(V.e) are shown in Fig. S9 [44].

The area of one pixel (k_0) is $0.89 \mu\text{m}^2$. Particle size k must be integer times of k_0 . Upon obtaining particle areas in an image, we generate the statistics by logarithmic binning [33]. Details of computations are in the Supplemental Material [44]. Particle size distributions of Expt. 1–14 are plotted in Fig. 3.

The power exponent in Fig. 3(a) is estimated by linear regression and the maximum likelihood method [33]. Agreement between the two methods can be reached, which yields $\alpha = 1.4$ [44]. In Fig. 3(b), the fraction of the smallest particles drops below the power-law trend. Moreover, data in the middle range are biased towards above the power-law trend. As confinement further decreases, a bimodal trend starts to form in Fig. 3(c) (note the left peak is not as pronounced as in bulk precipitations because the chip is still confined in vertical dimension). Additionally, its tail decays faster than the power-law trend. These features are characteristic of precipitation in bulk conditions. Therefore, we confirm that confinement is responsible for the power-law statistics.

To understand the origin of the statistics, we find the Yule process [33,39] useful. It describes the growth of a set of objects, which might be genera, cities, particles, etc. The object has a property k —such as the number of species in the genus, size of the particle, etc.; the object emerges while

existing objects grow larger in k . The Yule process predicts that if the addition of a new object and growth of existing objects persist, in the long-time limit, the objects' sizes observe a power-law distribution. To illustrate in a formal way, let us define several variables. (i) When a particle first appears, its size is the unit area k_0 . (ii) Between the appearance of the n th and $(n+1)$ th particle, m unit areas are added from the liquid phase due to supersaturation-driven particle growth. Therefore, total area at n is $S_T = n(m+1)k_0$. n increases linearly and measures the system's time [33], which we refer to as the Yule time. (iii) Dimensionless area $\theta = k/k_0$. (iv) The probability to have a particle of area θ at n is $p_{\theta,n}$.

In Newman's approach for the Yule process [33], the probability that when adding species (in our case, unit area) to the genera (in our case, particles) a genus (particle) with size θ_i gains one more species is $(\theta_i / \sum_i \theta_i) = [\theta / n(m+1)]$ (richer-get-richer). Since m unit areas are added, the probability that a particle of size θ gains a unit area is $[m\theta / n(m+1)]$ and the expected number of changes is $[m / (m+1)]\theta p_{\theta,n}$, which can be used to construct a master equation of $p_{\theta,n}$ [33]. A solution of the equation leads to the stationary distribution of $p_\theta = (1 + 1/m)\mathbf{B}(\theta, 2 + 1/m)$, where $p_\theta = \lim_{n \rightarrow \infty} p_{\theta,n}$ is termed the Yule distribution [40]. $\mathbf{B}(x, \alpha)$ is the beta function with parameter α , which scales as $x^{-\alpha}$ for large x .

Since m is positive, the exponent $(2 + 1/m)$ cannot equal to 1.4, as found experimentally; therefore, the model must be missing important phenomena. From experimental measurements, we find that the actual particle number does not increase linearly like the Yule time. In most cases the increase of particle number slows down at late times, and some even show a decrease, as shown in Fig. 4. In contrast, the total area continues to climb in all cases. The only explanation is mass transfer from small particles to large particles, i.e., ripening [45]. A direct visual example of the growth and ripening process is shown in Figs. 4(k)–4(p).

Small particles have higher surface energy than large particles due to larger surface curvature (the Kelvin

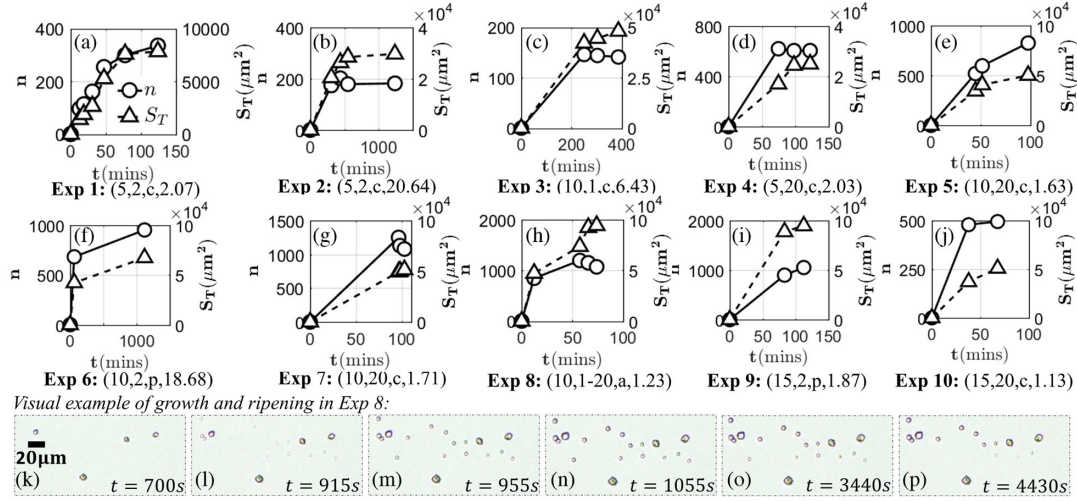


FIG. 4. Total area (S_T) and total number (n) of the crystal population versus time in Expt. 1–10, plotted in (a)–(j). Exact values behind the symbols are summarized in Tables S3–S12 [44]. As in Fig. 2, experimental conditions are attached to the plots. (k)–(p) show a sequence of growth and ripening in a region of size $200 \mu\text{m} \times 93 \mu\text{m}$ captured in Expt. 8.

equation [53]), which leads to higher equilibrium solute concentration around them than that around a large particle. This establishes the chemical potential difference for diffusion of solute from small particle to large particle during ripening. Therefore, in ripening large particles grow at the dissolution of small particles. On the other hand, supersaturation drives nucleation and solute deposition onto solids, and hence compensates for the loss from small particles, which leads to growth of all particles. However, when the difference between particle size (curvature) increases during the overall growth, it is increasingly difficult to compensate for the loss and the small particles will be dissolved. Simply put, growth fuels inequality, and inequality enhances ripening. In early times, from Figs. 4(k)–4(n), both the number and size of particles grew. From Figs. 4(n)–4(p), some particles became smaller, and some were dissolved, while the large ones kept growing. These direct visuals corroborate that ripening becomes important at late times while growth dominates at early times, thus explaining the trends in Figs. 4(a)–4(j).

We therefore introduce a ripening rate m_r , which is the number of unit areas that are transferred from small to large particles between the n th and $(n+1)$ th Yule time. We assume that the new transition probability is $[(m+m_r)\theta/n(m+1)]$. Since the net gain of area from liquid to solid phase is m , an extra flux m_r can only come from an existing solid phase, which may decrease the number of small particles. We rewrite the master equation [33] as

$$(n+1)p_{\theta,n+1} = np_{\theta,n} + \frac{(m+m_r)(\theta-1)}{m+1} p_{\theta-1,n} - \frac{(m+m_r)\theta}{m+1} p_{\theta,n}. \quad (1)$$

Solving for the stationary p_θ , we get [44]

$$p_\theta = (\alpha-1)\mathbf{B}(\theta, \alpha), \quad (2)$$

where the exponent reads

$$\alpha = 1 + \frac{m+1}{m+m_r}. \quad (3)$$

Obviously, if m_r vanishes, Eqs. (2) and (3) recover the classical Yule distribution and exponent. Importantly, Eq. (3) shows that a ripening flux m_r leads to a power exponent smaller than 2.

Mass transfer during precipitation in confinement is very difficult to measure experimentally [28] and m_r may not be directly measured either. However, m is measurable. More specifically, the slope of the total solid area S_T versus particle number n is $(m+1)k_0$. Data from Fig. 4 are used to generate plots of S_T versus n , shown in Fig. 5.

With m measured, m_r can be calculated from Eq. (3) as

$$m_r = \frac{2-\alpha}{\alpha-1} \cdot m + \frac{1}{\alpha-1}, \quad (4)$$

where α is known from the statistics [Fig. 3(a)]. Based on measurements in Fig. 5, calculated values of m_r for Expt. 1–10 are 39, 241, 63, 528, 115, 109, 75, 124, 159, and 154. Given that α is between 1 and 2, Eq. (4) indicates that higher growth rate leads to stronger ripening flux. Note that $(m+1)k_0$ is also the average particle size, and measurements in Fig. 5 indicate it is unbounded. This is compatible with a power exponent between 1 and 2, which causes a diverging mean [33].

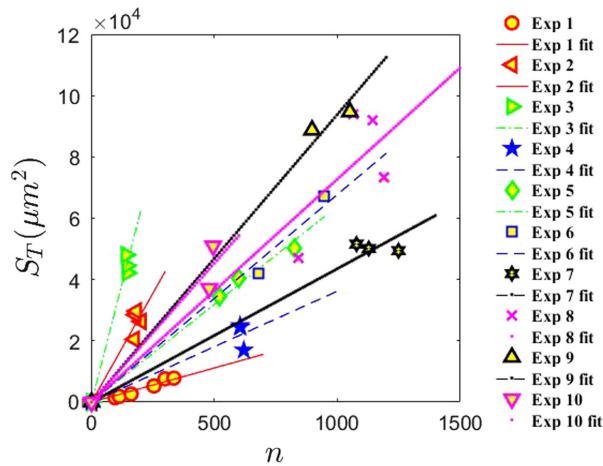


FIG. 5. Total area of the particles versus particle number in Expt. 1–10.

In conclusion, we demonstrate through microfluidic experiments that calcium carbonate precipitation in micrometer confinement obeys a power-law particle size distribution. The power-law behavior is explained by an extended Yule process with a ripening effect. The discovery offers new insight into the phenomenon of precipitation in confinement and may be useful in areas such as precipitation in porous media and material synthesis. Furthermore, the extended Yule process may find wide applications in natural and social systems. For example, the original Yule process could not consider extinction of species in its treatment of the biologic system [33]. In our model, agents can decrease in scale and disappear, which naturally allows “extinction” to occur. In many economies, the sizes of companies (measured by the number of employees) were found to observe power-law distributions with exponents smaller than 2 [54]. This may be explained by the extended Yule process since ripening could very well model the acquisition of small companies by large companies. In Earth sciences, the areas of wildfires and volumes of rain clusters were found to observe power-law distributions with exponents smaller than 2 [34], which might also relate to the extended Yule process. In general, we expect our model to be applicable when both growth and ripening are present.

* xujp@utexas.edu

[1] R. A. Berner, A. C. Lasaga, and R. M. Garrels, *Am. J. Sci.* **283**, 641 (1983).
 [2] J. C. G. Walker, P. B. Hays, and J. F. Kasting, *J. Geophys. Res.* **86**, 9776 (1981).
 [3] D. M. Raup, *J. Geol.* **67**, 661 (1959).
 [4] J. Aizenberg, M. Ilan, S. Weiner, and L. Addadi, *Connect. Tissue Res.* **34**, 255 (1996).
 [5] F. W. Tegethoff, J. Rohleder, and E. Kroker, *Calcium Carbonate: From the Cretaceous Period Into the 21st Century* (Springer, Basel AG, 2001).

[6] A. Borrego-Sánchez, R. Sánchez-Espejo, B. Albertini, N. Passerini, P. Cerezo, C. Viseras, and C. I. Sainz-Díaz, *Pharmaceutics* **11**, 533 (2019).
 [7] P. O. Roehl and P. W. Choquette, *Carbonate Petroleum Reservoirs* (Springer, New York, NY, 1985).
 [8] A. L. Boskey, *Connect. Tissue Res.* **44**, 5 (2003).
 [9] H. A. Lowenstam and S. Weiner, *On Biomineralization* (Oxford University Press, New York, 1989).
 [10] S. Mann, *Biomineralization: Principles and Concepts in Bioinorganic Materials Chemistry* (Oxford University Press, New York, 2001).
 [11] Y.-S. Jun, D. E. Giammar, and C. J. Werth, *Environ. Sci. Technol.* **47**, 3 (2013).
 [12] C. I. Steefel, S. Molins, and D. Trebotich, *Rev. Mineral. Geochem.* **77**, 259 (2013).
 [13] H. Ping, H. Xie, and Z. Fu, *J. Materiomics* **3**, 83 (2017).
 [14] S. Jaho, G. D. Athanasakou, V. Sygouni, M. G. Lioliou, P. G. Koutsoukos, and C. A. Paraskeva, *Cryst. Growth Des.* **16**, 359 (2016).
 [15] H. Yoon, K. N. Chojnicki, and M. J. Martinez, *Environ. Sci. Technol.* **53**, 14233 (2019).
 [16] C. Zhang, K. Dehoff, N. Hess, M. Oostrom, T. W. Wietsma, A. J. Valocchi, B. W. Fouke, and C. J. Werth, *Environ. Sci. Technol.* **44**, 7833 (2010).
 [17] J. Xu and M. T. Balhoff, *Lab Chip* **22**, 4205 (2022).
 [18] J. Xu and M. T. Balhoff, *Adv. Water Resour.* **164**, 104200 (2022).
 [19] D. Kim, N. Mahabadi, J. Jang, and L. A. v. Paassen, *Water Res. Res.* **56**, e2019WR025420 (2020).
 [20] C. Noiriell, C. I. Steefel, L. Yang, and D. Bernard, *Adv. Water Resour.* **95**, 125 (2016).
 [21] C. J. Stephens, S. F. Ladden, F. C. Meldrum, and H. K. Christenson, *Adv. Funct. Mater.* **20**, 2108 (2010).
 [22] M. Nooraiepour, M. Masoudi, and H. Hellevang, *Sci. Rep.* **11**, 16397 (2021).
 [23] T. W. Willingham, C. J. Werth, and A. J. Valocchi, *Environ. Sci. Technol.* **42**, 3185 (2008).
 [24] G. Schuszter, F. Brau, and A. D. Wit, *Phys. Chem. Chem. Phys.* **18**, 25592 (2016).
 [25] G. Schuszter, F. Brau, and A. D. Wit, *Environ. Sci. Technol. Lett.* **3**, 156 (2016).
 [26] F. C. Meldrum and H. Cölfen, *Chem. Rev.* **108**, 4332 (2008).
 [27] E. Loste, R. J. Park, J. Warren, and F. C. Meldrum, *Adv. Funct. Mater.* **14**, 1211 (2004).
 [28] F. C. Meldrum and C. O’Shaughnessy, *Adv. Mater.* **32**, 2001068 (2020).
 [29] B. Feng, A. K. Yong, and H. An, *Mater. Sci. Eng.* **445–446**, 170 (2007).
 [30] W.-M. Jung, S. H. Kang, K.-S. Kim, W.-S. Kim, and C. K. Choi, *J. Cryst. Growth* **312**, 3331 (2010).
 [31] J. Hostomsky and A. G. Jones, *J. Phys. D* **24**, 165 (1991).
 [32] Y. Kojim, K. Yamaguchi, and N. Nishimiya, *Ultrason. Sonochem.* **17**, 617 (2010).
 [33] M. E. J. Newman, *Contemp. Phys.* **46**, 323 (2005).
 [34] Á. Corral and Á. González, *Earth and Space Sci.* **6**, 673 (2019).
 [35] D. Marković and C. Gros, *Phys. Rep.* **536**, 41 (2014).
 [36] S. N. Dorogovtsev, J. F. F. Mendes, and A. N. Samukhin, *Phys. Rev. Lett.* **85**, 4633 (2000).

- [37] P. L. Krapivsky, S. Redner, and F. Leyvraz, *Phys. Rev. Lett.* **85**, 4629 (2000).
- [38] G. K. Zipf, *Human Behavior and the Principle of Least Effort* (Addison-Wesley Press, Inc., New York, 1949).
- [39] G. U. Yule, *Phil. Trans. R. Soc. B* **213**, 21 (1925).
- [40] H. A. Simon, *Biometrika* **42**, 425 (1955).
- [41] D. D. S. Price, *J. Am. Soc. Inf. Sci.* **27**, 292 (1976).
- [42] A.-L. Barabasi and R. Albert, *Science* **286**, 509 (1999).
- [43] C. Castellano, M. Marsili, and A. Vespignani, *Phys. Rev. Lett.* **85**, 3536 (2000).
- [44] See Supplemental Material at <http://link.aps.org/supplemental/10.1103/PhysRevLett.131.034001> for additional experimental and computational details and supplemental figures, which includes Refs. [27,33,45–49].
- [45] P. Bots, L. G. Benning, J.-D. Rodriguez-Blanco, T. Roncal-Herrero, and S. Shaw, *Cryst. Growth Des.* **12**, 3806 (2012).
- [46] Y. Zeng, J. Cao, Z. Wang, J. Guo, and J. Lu, *Cryst. Growth Des.* **18**, 1710 (2018).
- [47] Y. Zeng, J. Cao, Z. Wang, J. Guo, Q. Zhou, and J. Lu, *Cryst. Growth Des.* **18**, 6538 (2018).
- [48] B. Myszka, M. Schüßler, K. Hurle, B. Demmert, R. Detsch, A. R. Boccaccini, and S. E. Wolf, *RSC Adv.* **9**, 18232 (2019).
- [49] Jens-Petter Andreassen, *J. Cryst. Growth* **274**, 256 (2005).
- [50] C. Ramakrishna, T. Thenepalli, and J. W. Ahn, *Korean Chem. Eng. Res.* **55**, 443 (2017).
- [51] T. Ogino, T. Suzuki, and K. Sawada, *Geochim. Cosmochim. Acta* **51**, 2757 (1987).
- [52] M. Zeng, Y.-Y. Kim, C. Anduix-Canto, C. Frontera, D. Laundry, N. Kapur, H. K. Christenson, and F. C. Meldrum, *Proc. Natl. Acad. Sci. U.S.A.* **115**, 7670 (2018).
- [53] H.-J. Butt, K. Graf, and M. Kappl, *Physics and Chemistry of Interfaces* (Wiley-VCH, Weinheim, 2006).
- [54] B. Fix, *PLoS One* **14**, e0215692 (2019).